Appl. Phys. B 68, 1085–1094 (1999) / DOI 10.1007/s003409900011

Applied Physics B
Lasers
and Optics

Invited paper

Recent advances in terahertz imaging

D.M. Mittleman[1], M. Gupta[1,*], R. Neelamani[1], R.G. Baraniuk[1], J.V. Rudd[2], M. Koch[3]

[1] Electrical and Computer Engineering Department, Rice University, MS-366, 6100 Main St., Houston, TX 77005, USA
(Fax: +1-713/524-5237, E-mail: daniel@rice.edu)
[2] Picometrix, Inc., P.O. Box 130243, Ann Arbor, MI 48113, USA
[3] Institut für Hochfrequenztechnik, Schleinitzstr. 22, Technical University of Braunschweig, D-38106 Braunschweig, Germany

Received: 29 January 1999/Published online: 7 April 1999

Abstract. We review recent progress in the field of terahertz "T-ray" imaging. This relatively new imaging technique, based on terahertz time-domain spectroscopy, has the potential to be the first portable far-infrared imaging spectrometer. We give several examples which illustrate the possible applications of this technology, using both the amplitude and phase information contained in the THz waveforms. We describe the latest results in tomographic imaging, in which waveforms reflected from an object can be used to form a three-dimensional representation. Advanced signal processing tools are exploited for the purposes of extracting tomographic results, including spectroscopic information about each reflecting layer of a sample. We also describe the application of optical near-field techniques to the THz imaging system. Substantial improvements in the spatial resolution are demonstrated.

PACS: 07.57.Pt; 42.65.Re

1 Terahertz time-domain spectroscopy

The far-infrared, or *terahertz*, region is one of the least explored ranges of the electromagnetic spectrum. Until relatively recently, it was difficult to efficiently generate and detect terahertz (THz) radiation. Most THz sources were either low-brightness emitters such as thermal sources, or cumbersome, single-frequency molecular vapor lasers. Detection usually relied on bolometric methods, which require cryogenic operation and generally provided low sensitivity.

Recently, however, there has been a revolution in THz technology, as a number of newly discovered or re-discovered generation and detection schemes have revitalized the field. These techniques, based on frequency conversion using nonlinear optics [1–6], are often simpler, more reliable, and potentially much less expensive than the more traditional approaches. One of the first and most interesting of these non-linear optical techniques is *terahertz time-domain spectroscopy*, or THz-TDS [7]. The key components of a THz-TDS system are a femtosecond laser and a pair of specially designed transducers. By gating these transducers with ultrafast optical pulses, one can generate sub-ps bursts of THz radiation, and subsequently detect them with high signal-to-noise. These THz transients consist of only one or two cycles of the electromagnetic field, and they consequently span a very broad bandwidth. Bandwidths extending from ≈ 100 GHz to 2 or 3 THz are routine, and more than 5 THz has been demonstrated [8]. Furthermore, although the average intensity of the radiation is quite low, the high spatial coherence produces a brightness that exceeds that of conventional thermal sources. Finally, the gated detection is orders of magnitude more sensitive than typical bolometric detection, and requires no cooling or shielding of any kind. The design, construction, and characterization of a THz-TDS system, including in particular the semiconductor transducers [7, 9, 10], has been described elsewhere [11, 12].

Due to the high signal-to-noise and broad bandwidth, the THz-TDS system is ideal for spectroscopic studies of many different physical systems. Many condensed-phase systems exhibit interesting phenomena in the THz spectral range, and, in many cases, these are not yet understood. Indeed, the THz-TDS system provides opportunities for spectroscopic studies that would not otherwise be possible. For example, the coherent detection permits the investigation of hot samples such as flames. These would be impossible to study using any detection system that is sensitive to the radiation from the sample. The coherent gated detection of the THz-TDS system is insensitive to incoherent radiation, and is therefore the only far-infrared system capable of flame spectroscopy [13]. A second example is the class of experiments which exploit the extremely short temporal duration of the THz pulses. A typical example is the 'visible-pump, THz-probe' experiment, in which a sample is optically prepared with a fs optical pulse, and the evolution of the far-infrared spectrum is measured

* *Present address*: Electrical Engineering Dept., Stanford University, Stanford, CA

with a time-delayed THz probe pulse. Numerous examples of this and similar techniques have been reported in the last few years [14, 15].

Perhaps even more interesting than the spectroscopic uses, the potential technological applications of THz-TDS have begun to attract considerable attention. This has been spurred in large part by the development of imaging systems based on THz-TDS [16–18]. The value of a practical far-infrared imaging system has been recognized for some time, in a wide range of applications [19–23]. Because THz-TDS does not require any cryogenics or shielding for the detector, it has the potential to be the first THz imaging system that is portable, compact, and reliable enough for practical application in "real-world" environments. In this article, we describe several recent advances in THz "T-ray" imaging.

2 T-ray imaging

The details of the T-ray imaging technique have been described in a number of recent publications [16, 17]. Here, we briefly review the highlights, and provide a few illustrative examples. In order to form images, the THz beam is brought to an intermediate focus using a pair of lenses or parabolic reflectors, which are inserted into the region where the THz beam is collimated. This is shown schematically in Fig. 1, where the lens pair is mounted on a plate which can be moved into or out of the collimated THz beam. High-resistivity silicon and high-density polyethylene are two excellent choices for lens materials. The former has no absorption or chromatic dispersion over the whole THz range, but has a high index (≈ 3.42) and therefore relatively large Fresnel losses [24]. The latter has lower Fresnel losses, but has some small absorption above 1 THz, and a measurable resonance at ≈ 2.2 THz [25].

One can place an object at the focus of the THz beam, and measure the waveform that has traversed through the object. By translating the object, and measuring the transmitted THz waveform for each position of the object, one can build an image pixel by pixel. Focal-plane imaging has also been demonstrated, using large-area electro-optic crystals for detection of the THz radiation [18]. The image formed in this fashion may represent any desired aspect of the measured waveforms, including amplitude [16, 17], phase [17], or any combination [26]. In order to form images in a reasonable time, the waveforms must be digitized and the desired information extracted on the fly. This can be accomplished using a commercial digital signal processor in a PC, which synchronizes the motion of the object through the focal spot with the waveform acquisition.

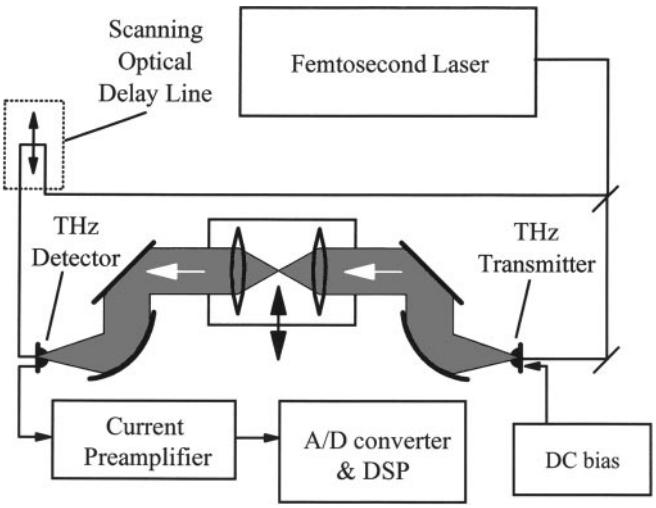

Fig. 1. A schematic of a THz-TDS system, showing the fs laser, scanning delay line, THz transmitter and detector, collimating optics, and associated electronics. A lens pair separated by $2f$ can be inserted into the collimated region of the THz beam, converting the system into a transmission imaging system with an intermediate focus

The list of possible applications of such a system is quite extensive. Perhaps the most promising applications lie in the area of quality control of packaged goods. Figure 2 shows a THz image of a $\approx$ 2-cm-square portion of a small (1–3/8 oz.) box of cereal. The cardboard box in which the cereal is packaged is nearly transparent to the THz radiation. The dark areas in the image are raisins, which exhibit a high contrast relative to the surrounding material due to their high water content. In this image, the thickness of the sample ($\approx$ 5 cm) is somewhat larger than the confocal parameter of the THz beam ($\approx$ 1 cm); as a result, the raisins (which were not situated at the THz beam focus) appear larger in the image than their actual size. Since one can in principle choose any set of THz beam optics for an imaging system, this effect should not substantially limit the utility of the technique. This imaging tool is well suited for inspection of sealed packages if the packaging is comprised of transparent materials such as cardboard, most plastics, thin pieces of dry wood, etc.

These types of applications are not limited to quality control of consumer products. Figure 3 illustrates the use of THz imaging for the inspection of artwork. Figure 3a is a visible image of a piece of parchment, upon which an inscription has been written. The inscription is painted over with a thick layer of black paint. The parchment is then imaged with T-rays, in an attempt to reveal the hidden writing. Because the black paint overlayer is not lead-based paint, it is transparent to THz radiation. Depending on the writing implement used to form the original inscription, the THz image may or may not show the underlying writing. Figure 3b shows a THz image of one sample, in which the original inscription ("OK") was written with a charcoal pencil. The thin graphite layer of writing on the parchment provides sufficient amplitude contrast to be visible in the THz image. Not surprisingly, if the inscription is written with conventional ink, one cannot detect it in the THz image, because the dye molecules in the ink are non-polar and thus do not absorb strongly in the THz range. This test suggests the possibility of using THz imaging for the investigation of underdrawings beneath paintings. This could be an excellent complimentary technology to the mid-infrared and X-ray imaging systems currently used for such studies. More broadly, one can imagine that this new technique could be useful in a wide range of fields including art history, archaeology, forensics, etc., in which one requires non-invasive methods for imaging. In this context, it is worth emphasizing that the power generated in the T-ray beam is extremely low, roughly $20 - 100$ times less than the same power emitted from a room-temperature blackbody in the frequency range 0–3 THz. Thus, the risks to delicate or sensitive samples are minimal.

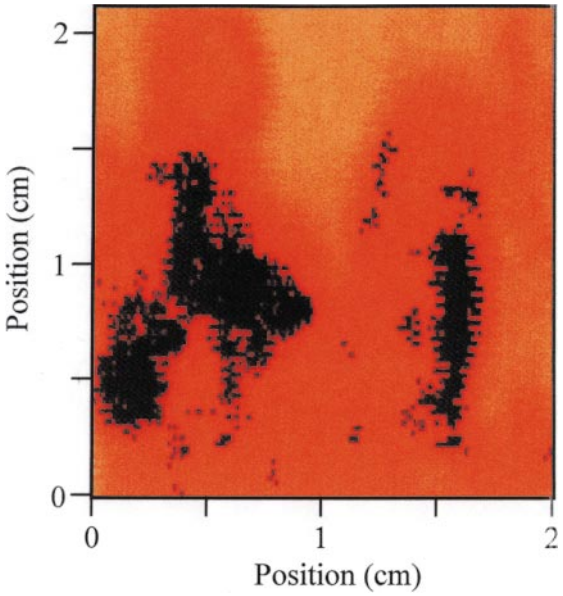

Fig. 2. THz transmission image of a ≈ 2-cm square portion of a small box of breakfast cereal. The false color scale is related to the transmitted THz amplitude. The *dark regions* are raisins. These appear somewhat distorted because the width of the sample is ≈ 5 times larger than the confocal parameter of the THz beam

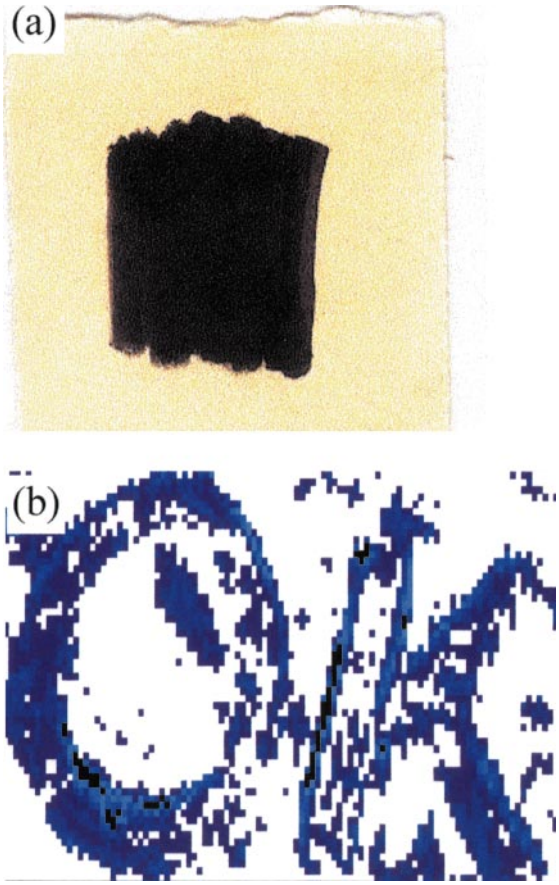

Fig. 3. a Visible image and **b** THz transmission image of a sample designed to mimic written text hidden beneath a layer of black paint. In **b**, the text is written with a charcoal pencil; this thin layer of graphite on the parchment provides sufficient contrast in transmitted THz amplitude to form a readable image. The image in **b** is approximately 2.5 cm square, and covers the central portion of the painted region in **a**

As mentioned above, it is possible to form images based on any aspect of the transmitted THz waveforms, not merely the amplitude. Figure 4 illustrates this, showing two THz images of a chocolate bar. In the upper image, the gray-scale is determined by the peak-to-peak amplitude of the THz pulse at each pixel, as in Figs. 2 and 3 above. The chocolate does not absorb much THz radiation, but several other features are visible. First, the sample has a plano-convex cross-sectional profile, and is therefore thinner at the top and bottom than in the middle. Second, the embossed letters are visible only because of scattering effects at their stepped edges, and as a result are rather difficult to read. Finally, because almonds absorb more THz radiation than chocolate, they can be easily detected using this technique; four almonds are visible in this image. The lower image shows the same sample, except that this image is formed using the arrival time (i.e., phase) of the THz pulse rather than the amplitude. Here, the image primarily contains information about the thickness of the sample at each point, so the embossed letters and the overall thickness variation are much more prominent. The almonds are nearly invisible, except for the very dark regions where the transmitted pulse was too small for an accurate determination of the arrival time.

Figure 4 demonstrates one way in which the phase information contained in the THz waveforms can be used to form images that contain different information from those encoded based on amplitude alone. This technique becomes even more powerful when the sample is imaged in a reflection geometry, rather than in transmission [27]. In this mode, one takes advantage of the pulse width (or, more precisely, the coherence length) of the THz pulses to generate three-dimensional representations of layered objects. The use of a reflection

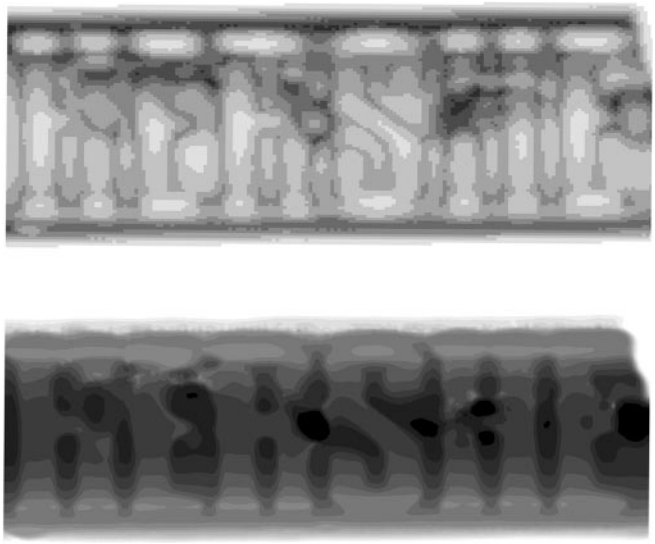

Fig. 4. Two THz images of a chocolate bar. The *upper image* shows the variation in amplitude of the transmitted waveform. Here, the embossed lettering is only visible because of scattering effects at the stepped edges of the embossing, whereas the almonds are clearly visible due to their stronger absorption of the radiation. The *lower image* shows the variation in transit time of the THz pulse, reflecting the accumulated phase. Here, the almonds are almost invisible, but the variation in the thickness of the sample is quite clear, allowing the embossed lettering to be easily discerned. The *darkest spots* on the *lower image* represent regions where the amplitude of the transmitted pulse was too small to make an accurate determination of the transit time

imaging system presents some unique challenges and capabilities, which are explored in detail below.

3 Reflection imaging with T-rays

3.1 Tomographic image reconstruction

An imaging system in which the THz beam is reflected off of the sample, rather than transmitted through it, can be used for tomographic imaging [27, 28]. Suppose that the beam reflects off of the sample at nearly normal incidence, and that the sample is thin compared to the confocal parameter. Then, if the sample consists of several well-separated dielectric layers, the interface between each pair of layers reflects a portion of the THz beam in a confocal geometry. The reflected waveform therefore consists of a series of isolated pulses. Each pulse in this pulse train contains information about each of the layers through which it propagated, as well as the interface from which it originated. Given the shape of the incident THz pulse and the complex dielectric function of the materials comprising each of the layers, one can predict this output waveform using conventional optics.

Figure 5 illustrates this using a ball-point pen as an example. Figure 5a shows the waveform obtained by placing a mirror at the reflection point, and thus represents the incident wave. The smaller oscillations that follow the main transient arise from a number of effects, including water vapor in the THz beam path [29], electrical impedance mismatch effects in the emitter and receiver antennas, and optical reflections in the antenna substrates. These are entirely repeatable and do not substantially interfere with the measurement. However, as discussed below, they can limit the effectiveness of signal processing algorithms used for data analysis. Figure 5b shows the waveform reflected from a ball-point pen. The pen is oriented such that its long axis is perpendicular to the propagation direction of the THz beam. Here, the eight pulses originate from reflections off of each of the eight interfaces which the beam encounters as it propagates through the two concentric plastic cylinders which comprise the pen. Because the sign of the dielectric discontinuity alternates (i.e., first from air to plastic, then from plastic to air), the polarity of the eight reflections alternates as well. Using the Fresnel coefficients for normal-incidence field transmission and reflection, one can derive a good approximation to the reflected waveform from the incident waveform $E_{\mathrm{in}}(t)$, Fig. 5a. For example, the first pulse in the train is given by

$$E_1(t) = \eta F^{-1}\left(\frac{n_1 - n_{\mathrm{air}}}{n_1 + n_{\mathrm{air}}}\mathcal{E}_{\mathrm{in}}(\omega)\,\mathrm{e}^{\mathrm{i}\Phi}\right), \tag{1}$$

and the second pulse is

$$E_2(t) = \eta F^{-1}\left(\frac{n_2 - n_1}{n_2 + n_1}\frac{4n_1}{(n_1 + n_{\mathrm{air}})^2}\mathcal{E}_{\mathrm{in}}(\omega)\,\mathrm{e}^{-2\mathrm{i}n_1\omega x_1/c}\,\mathrm{e}^{\mathrm{i}\Phi}\right). \tag{2}$$

Similar expressions can be derived for each of the eight reflections. In (1) and (2), F^{-1} represents the inverse Fourier transform, and $\mathcal{E}_{\mathrm{in}}(\omega)$ is the Fourier transform of the input waveform $E_{\mathrm{in}}(t)$. The refractive index of the material comprising the jth layer is n_j, with $n_0 = n_{\mathrm{air}}$. Φ is a constant phase factor which accounts for the difference between the position of the pen and the position of the mirror used to obtain $E_{\mathrm{in}}(t)$. η is a geometrical factor which accounts for the difference in detection efficiency between Figs. 5a and 5b. This results from the fact that in one case the reflector is

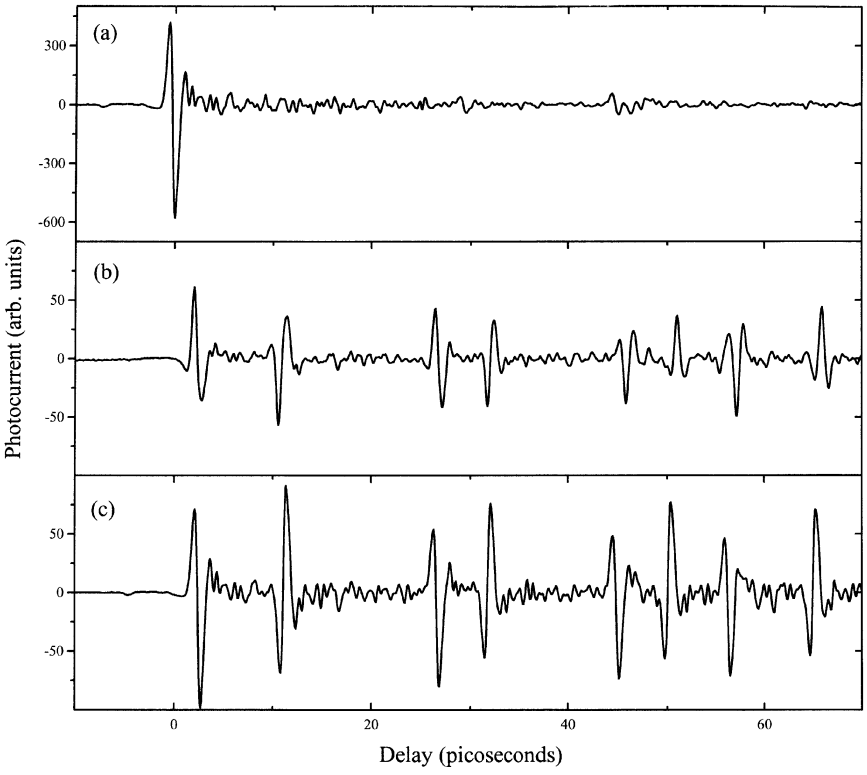

Fig. 5a–c. THz waveforms reflected off of **a** a reference mirror, and **b** a ball-point pen oriented so that its long axis is perpendicular to the THz beam propagation direction. **c** A simulation of curve **b**, using curve **a** as the input wave, generated as described in the text

planar whereas in the other the reflections all arise from cylindrical surfaces.

One can estimate the size of η using a ray matrix approach. First, we assume that the input is a Gaussian beam, with a flat phase front and a 25-mm-diameter beam waist at $z = 0$, the location of the focusing optic. We assume that the mirror, used in place of the sample in obtaining the data of Fig. 5a, is located at the focal spot of this lens, at $z = d_1 \approx f - z_R^2/f$. Here, z_R is the Rayleigh range of the focused beam [30]. The beam reflects off of the mirror, and returns back to $z = 0$, having traveled a distance of $2d_1$. The beam must then propagate an additional $d_2 \approx 0.5$ m before encountering an aperture, in the form of the lens which focuses it onto the THz detector. The collection efficiency is the fraction of the initial field that reaches the detector. This can be found by integrating the field amplitude at the aperture. We perform this calculation for two cases: a planar mirror at $z = d_1$ and a cylindrical reflector at $z = d_1 - \delta$. If the sample is symmetrically placed with respect to $z = d_1$, then the convex front surface at $z = d_1 - \delta$ has a radius of curvature of $R = -\delta \approx -3.5$ mm. The parameter η is the ratio of the collection efficiencies of the electric fields in the two cases.

Because R is comparable to λ for some wavelength components of the THz pulse, diffraction effects are significant, and η therefore depends on λ. We calculate η for all wavelength components within the bandwidth of the radiation, and then calculate an average value weighted by the amplitude spectrum of the input pulse. Using this procedure, we find a value of $\eta = 0.79$ for the values of R and δ specified above. This value is used in the calculation of all eight reflected pulses. The result is displayed in Fig. 5c, on the same vertical scale as Fig. 5b. In this simulated result, the refractive indices of the outer and inner plastic cylinders are taken to be $n_1 = n_7 = 1.5$, and $n_3 = n_5 = 1.4$, respectively. The choice of these values is motivated by the results displayed in Fig. 6, below; they are close to the known far-infrared refractive indices of similar polymer materials such as Teflon ($n \approx 1.45$) and polypropylene ($n \approx 1.50$) [31]. Clearly, the simulation reproduces the experimental result qualitatively, although the amplitudes of the reflections are somewhat overestimated, and there is some pulse reshaping which is not accurately reproduced.

In principle, one could use the full wavelength-dependent form for η in (1), (2), and the other six similar expressions. Further, η is different for each of the eight reflections, since each has its own associated values for R and δ. Also, η is in general a complex quantity, due to the effect of the Guoy phase shift on a focused beam [32]. However, these concerns go beyond the spirit of the paraxial approximation which is the basis for the ray matrix formalism. The difficulties associated with using geometrical optics to describe scattering from objects of size comparable to λ are well known, and have even been discussed in the context of THz-TDS [33].

One might be able to further improve and refine the simulations of tomographic data using more sophisticated models. However, we are more interested in developing methods for extracting information about the sample directly from the measured data. This is more relevant for the purposes of many of the applications mentioned above. In order to proceed along these lines, one must solve an inverse problem: given the incident and reflected THz waveforms, determine the nature of the sample, particularly the refractive index profile. In the case under consideration, this profile is evidently step-like, alternating between n_{plastic} and n_{air}. The fundamental challenge is to develop an algorithm that locates the sizes and positions of the steps in this profile.

In an earlier work [27], we described a simple algorithm for generating this index profile from measured data, based

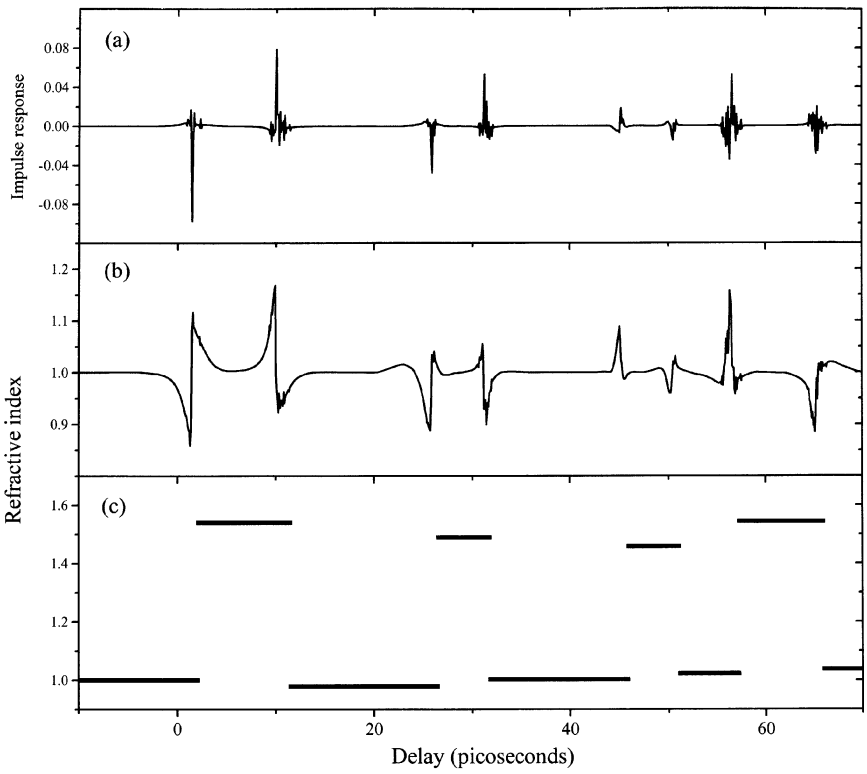

Fig. 6. **a** Impulse response of the sample derived from the waveforms of Figs. 5a and 5b, using a procedure outlined in the text. **b** Refractive index profile derived from **a**, using the method of [27]. **c** Refractive index profile derived directly from the data of Fig. 5b, using the stabilized numerical approach described in the text. The deconvolved impulse response of **a** was *not* used in calculating curve **c**

on an iterative application of the Fresnel coefficients. This algorithm was only an approximate result, as it neglected both absorptive and dispersive effects, as well as the finite bandwidth of the THz pulse. It provided an average refractive index in each step, where the average was over all frequencies within the bandwidth of the pulse.

One would ideally like to include absorption and dispersion in such an algorithm, as well as a method for extracting the *frequency-dependent* index $n(\omega)$ of each layer, rather than simply an average index. Also, a more numerically stable approach is required. This can be illustrated by applying the simple algorithm of [27] to the data of Fig. 5b. To do so, one must first deconvolve the bipolar response characteristic of the THz pulses, using Fig. 5a as a reference. The result of this deconvolution represents the impulse response of the layered medium, and ideally consists of a series of delta functions of varying height and polarity. However, due to the ringing which follows the main transient, mentioned above, this deconvolution procedure is somewhat complicated. It is necessary to implement a wavelet-based denoising on both the signal and the reference prior to the deconvolution, a procedure which is well suited for time-domain signals of this type [34]. The result is again wavelet filtered to remove low-amplitude noise and a low-frequency background. This final deconvolved waveform is shown in Fig. 6a. This appears to be a reasonable approximation to the ideal impulse response function, and one might anticipate that the algorithm of [27] might be sufficient to extract a useful index profile. However, the extended wings and ringing which appear on either side of each of the eight spikes lead to severe problems. The index profile derived in this fashion is shown in Fig. 6b, highlighting the numerical instability of this simple approach.

In order to deal with this difficulty, we have developed a more numerically stable approach, which is also far more amenable to incorporation into an automated routine. This approach does not make use of the deconvolution procedure mentioned above, and therefore does not require the intermediate step illustrated in Fig. 6a. Instead, we first use a peak-picking routine to identify the interfaces directly from the reflected time-domain waveform (i.e., Fig. 5b). Thus, the interfaces are necessarily abrupt, an immediate improvement over the earlier technique. Then, using the Fresnel coefficients, the refractive index on one side of the interface is related to the index on the other side. Given the index of the initial layer (air), one can iterate through the waveform and solve for each layer's index successively. This involves a windowed Fourier transform of the particular pulse in question, followed by a deconvolution of the input pulse. This gives the full frequency-dependent index of each layer, assuming that the absorption coefficient $\alpha(\omega)$ is negligible.

The deconvolution of the input pulse is not simply a ratio in the Fourier domain, as in Fig. 6a, above. Rather, it is necessary to first ensure that the denominator in this ratio is stable and causal and thus invertible with a stable causal filter. We use a cepstral analysis [35] to decompose the original system into two components. The first is minimum phase (having all transfer function zeros inside the unit circle of the z-transform plane [35]) and thus is both stable and causal when inverted. The second is allpass (having a transfer function with flat magnitude response) and is neither stable nor causal when inverted. Only the magnitude-equivalent minimum-phase system is used in the analysis. The deconvolved result is then denoised using a wavelet thresholding with Haar wavelets [36].

The result of this procedure, in which the average value of $n(\omega)$ is displayed for each of the layers, is shown in Fig. 6c. These values also take into account the geometrical factor η described above, since the measured reflected fields are all proportional to this factor. This index profile is evidently far more realistic than the one derived using the earlier approach (Fig. 6b), and the index values for the plastic layers are reasonable. Presently, we are working on improving the accuracy and stability of the procedure, in part by modifying the processing to include the possibility of a non-zero absorption coefficient. If $\alpha(\omega)$ is not negligible, then the index at each interface is no longer an analytic function of the windowed, deconvolved pulses, and further numerical processing is required [37]. Even with this additional complication, the denoising threshold parameter is essentially the only aspect of the analysis that requires "tweaking" on a case-by-case basis. So, the procedure holds great promise for implementation in a real-time processing package.

3.2 Tissue burn reflectometry

The techniques described above are applicable to situations where the sample under study consists of a number of discrete, relatively well separated dielectric layers. Another possible use of THz reflection imaging is in the area of biomedical diagnostics, where the samples may only consist of one reflecting surface, but with far more complex morphology. An example of an application in this area is the study of surface or near-surface skin properties, such as in the diagnosis of burn depth and severity. A reliable non-invasive probe of burn depth would be of great value to clinicians, who currently have no such technology. The application of optical probes to this problem has been an active research area recently [38].

Here, we present preliminary data using chicken breast as a model tissue system. The tissue is burned using an argon ion laser, producing a series of circular burns of increasing severity. Figure 7 shows a terahertz reflection image of one

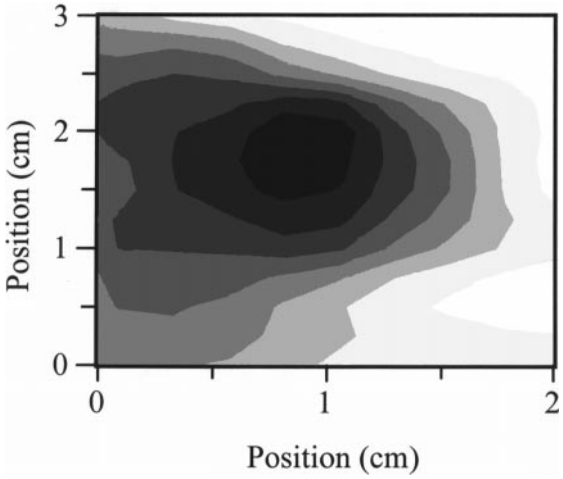

Fig. 7. THz reflection image of a circular burned region on a tissue sample (chicken breast). The false color scale corresponds to the reflected THz amplitude in the frequency range 0.5–1.0 THz. *Darker shades* indicate less reflected radiation

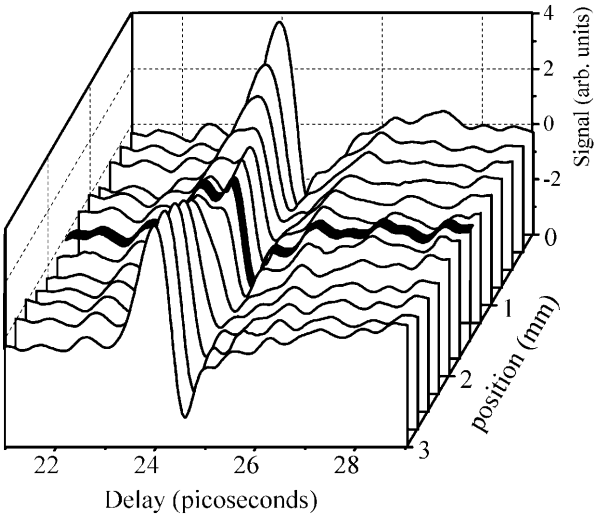

Fig. 8. THz waveforms reflected from a series of equally spaced points along a line through the center of a burn such as the one depicted in Fig. 7. The waveforms at either end of the series are both reflected from undamaged tissue, and are thus nearly equivalent to one another. The central waveform (*thick line*) is reflected from the center of the burned region, and is strongly distorted by the damage-induced changes in the tissue's THz optical properties

such burn; here, the reflected THz energy is displayed in gray scale, with the center of the burn reflecting the least. Figure 8 shows a series of waveforms obtained by translating the sample relative to the THz spot, in 250-μm steps. The central waveform $E_{\mathrm{cent}}(t)$ (thick line) was reflected off of the center of the burn, while the waveforms at either end of the series (E_{end1} and E_{end2}) originated from reflections off of undamaged tissue on either side of the burn. The distortions imposed upon E_{cent}, relative to E_{end1} and E_{end2}, reflect the modifications in the THz optical properties of the tissue as a result of the burn.

We may analyze the waveform distortions by comparing E_{cent} to E_{end1} in the frequency domain. Figure 9 shows this comparison in both amplitude and phase. For reference, the two end waveforms are compared to each other as well. In Fig. 9a, it is clear that $|E_{\mathrm{cent}}/E_{\mathrm{end1}}|$ is substantially less than one, and decreases with increasing frequency. This explains the relatively restricted bandwidth of this measurement; above 1 THz, the waveform reflected from the burn is attenuated to below the noise limit. Figure 9b shows that the relative phase of the two waveforms is also modified by the properties of the burned tissue, at least below 0.7 THz. The reasons for these modifications of $n(\omega)$ and $\alpha(\omega)$ remain unclear, although they cannot be attributed solely to changes in surface water content [39]. A number of chemical and morphological modifications occur when tissue is burned, and any one or a combination of several factors could be responsible. The fact that distinct, frequency-dependent effects are observable is an encouraging indication of the potential value of this technology.

4 THz near-field imaging

In forming the images shown in Fig. 4 above, large (200 μm) THz antennas were used, so the spectral bandwidth of the

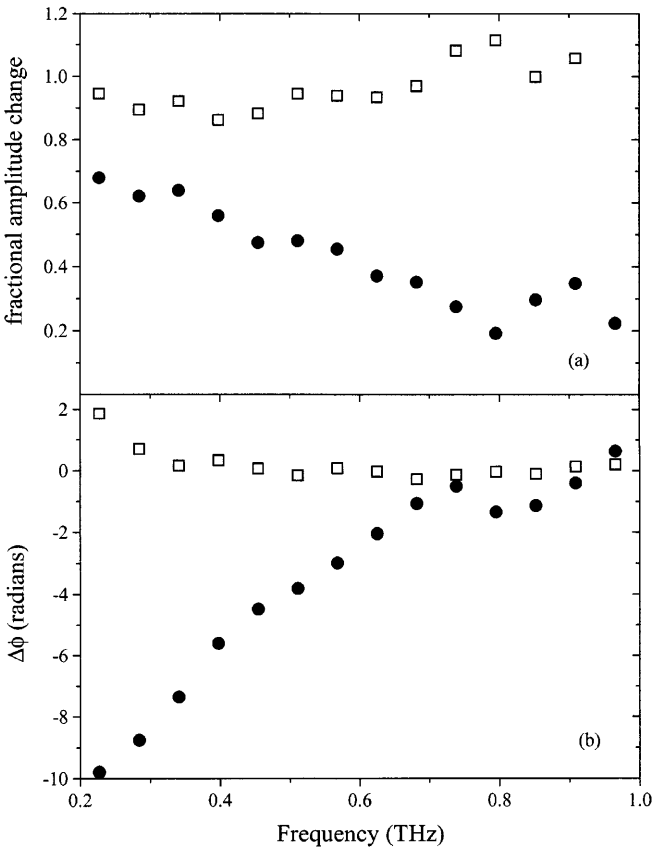

Fig. 9a,b. A comparison of the differences in **a** amplitude and **b** phase between the central and end waveforms in Fig. 8. In both cases, the *solid circles* represent $E_{\mathrm{cent}}/E_{\mathrm{end1}}$, and the *open squares* represent $E_{\mathrm{end2}}/E_{\mathrm{end1}}$. Here, E_{cent} is the central (*thick line*) waveform from Fig. 8, corresponding to position 1.5 mm. E_{end1} and E_{end2} are the waveforms at positions 0 and 3 mm, respectively

pulses barely exceeded 1 THz. As a result, the average wavelength of the radiation is larger than in the cases shown in Figs. 2 and 3. Consequently, the spatial resolution is lower, only 0.5 mm. In the images presented above, this resolution is sufficient to show all of the important features in the images, but other applications may require higher resolution. One route for improving the spatial resolution is near-field imaging [40].

According to Abbe's law the spatial resolution that can be achieved when imaging with electromagnetic waves is limited by the wavelength of the employed radiation. Of course, since the wavelength varies by more than one order of magnitude over the bandwidth of the THz pulses, the resolution in T-ray imaging depends on the spectral range over which the integration is performed to obtain a pixel. One obvious way to improve the resolution is to form the image based on the information contained in the highest frequency components of the measured waveforms. This can be accomplished using the signal processing hardware mentioned above. For each pixel, a waveform is acquired, an FFT is performed, and the high-frequency portion of the resulting amplitude spectrum is integrated. The ultimate limitation of this technique lies in the exponentially decreasing signal amplitude at high frequencies, leading to a trade-off between spatial resolution and signal-to-noise. For the THz imaging setup described above, this

has so far limited the resolution to about 0.25 mm [16], as in Fig. 3b.

In the following we show that the spatial resolution of the imaging setup can be considerably enhanced by applying the concepts of near-field microscopy [41, 42]. The basic idea is to insert a near-field tip into the intermediate focus of the imaging setup [40]. Essentially, the tip represents an aperture with a diameter that is smaller than the diffraction-limited beam waist.

In these experiments, the tips were produced by electroplating several mm of Cr/Ni onto sharp aluminum tips. After pulling the aluminum tip out of the resulting Cr/Ni cone, the cone is polished from its tip side until breakthrough. This produces a funnel-like Cr/Ni cone which has an entrance aperture larger than the diameter of the intermediate focus and a near-field aperture of typically 100 μm or less. This tip is positioned in the intermediate focus, with the small aperture pointing towards the receiver antenna. Samples are then moved directly in front of the near-field aperture.

The first near-field image that has been taken is shown in Fig. 10a. The dark rectangular shape in the middle shows the two contact pads of a broken silicon-on-sapphire antenna. Together they have a size of 0.5 by 1.0 mm. The small gap between the pads and the striplines connecting to the dipole are still too small to be resolved. The vertical structures to the left and right represent the edges of the sapphire substrate. The enhanced resolution of the THz near-field image becomes obvious when compared with a conventional transmission image. In this image (Fig. 10b), the contact pads are much less well resolved.

To demonstrate the enhanced resolution more quantitatively, a razor blade is translated across the beam profile, in front of the near-field tip. The solid line in Fig. 11 shows the

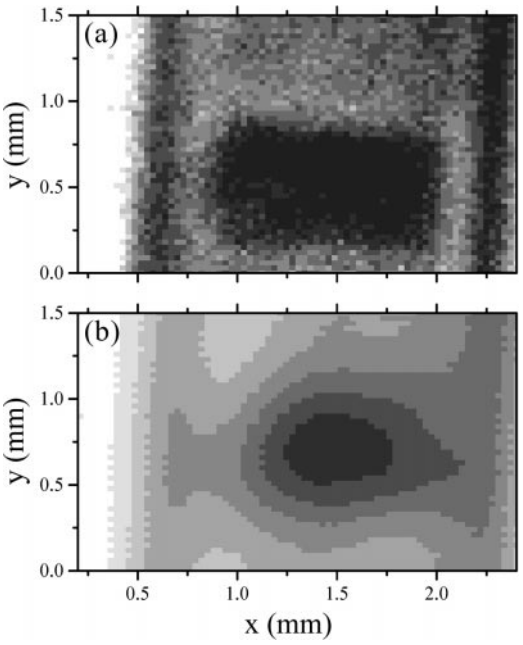

Fig. 10a,b. THz-images of two adjacent gold contact pads of a photoconductive antenna structure. **a** near-field image using a 100-μm aperture as described in the text, **b** standard T-ray transmission image. The use of the aperture dramatically enhances the spatial resolution of the imaging, permitting a much clearer resolution of the sample

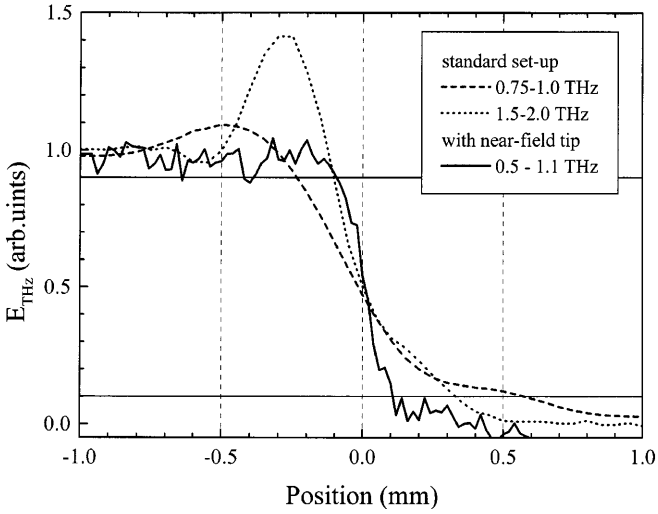

Fig. 11. T-ray line-scans over a razor blade with near field tip (*solid line*) and after removing the tip (*dashed and dotted lines*). The *horizontal lines* show the 10%–90% rise of the signals

drop in THz amplitude as a function of the position of the blade. These data are extracted by integrating the transmitted waveform from 0.5 to 1.1 THz, a region with a (weighted) mean wavelength of ≈ 390 μm. These data show a rise from 10% to 90% within about 200 μm. This value corresponds to twice the aperture diameter of 100 μm. For an integration between 1.1 and 2.0 THz, the 10%–90% distance drops to 140 μm [43]. For comparison we remove the tip and slide the razor blade through the empty focus. Two resulting line-scans for integration between 0.75–1.0 THz and 1.5–2.0 THz are shown as dashed and dotted lines, respectively. Although the average wavelength in these scans is substantially lower, the 10%–90% distance is larger than 200 μm for both curves. Moreover, both line-scans do not represent simple step functions but show an "overshoot" for negative positions of the razor blade. We attribute this additional feature to diffraction of the THz radiation at an edge. The introduction of the near-field cone leads to a considerable reduction of the detected THz amplitude. Yet, since we detect here the electric field amplitude and not the radiation intensity, the signal reduction is not so severe as one would encounter in the equivalent optical near-field imaging experiment. The resulting signal is still large enough for forming images.

Figure 12a shows a THz waveform transmitted through the tip in comparison with a reference waveform taken after removing the tip. The transmitted waveform has been magnified seventy-fold to roughly match the amplitude of the reference waveform. The signal decrease by a factor of 70 observed here corresponds to an intensity drop of ≈ 5000, which is a typical value for optical near-field microscopy [41, 42]. Smaller near-field apertures lead to a further lowering of the THz amplitude. For an elliptical aperture of 50×80 μm, we find a signal reduction by a factor of 130 [40].

A close comparison of the transmitted waveform with the reference reveals an additional effect of the near-field tip. Obviously the transmitted waveform shows much faster and more pronounced oscillations. This indicates that the near-field cone acts as a high-pass filter. The filter effect arises from the fact that the high-frequency THz radiation focuses more tightly than the lower frequency components.

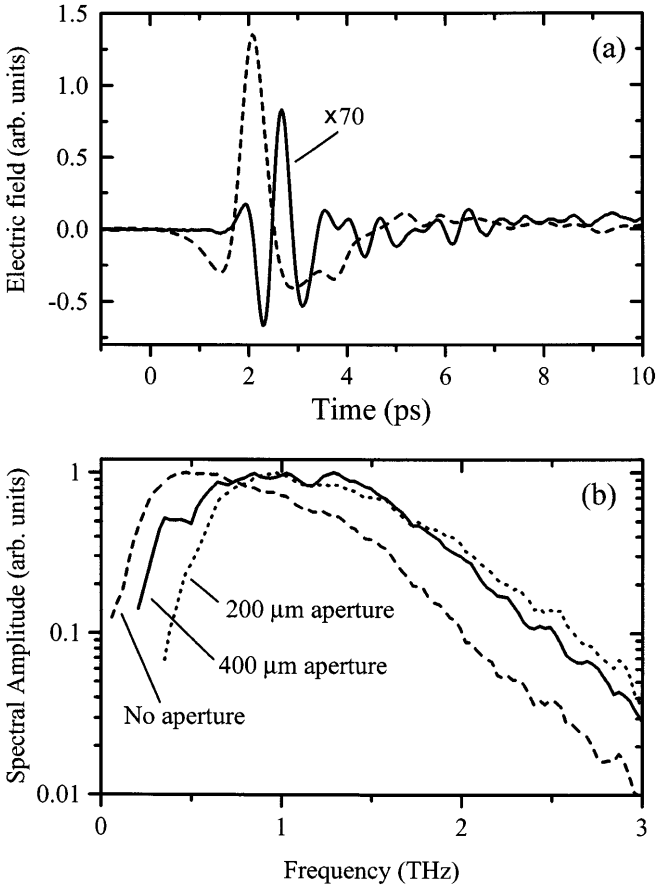

Fig. 12. a THz waveform transmitted through the near-field tip (*solid line*) and reference waveform (*dashed line*) taken without the tip. The pulse reshaping is a result of the high-pass filtering effect of the tip. The waveform transmitted through the tip has been scaled by a factor of 70. **b** Normalized spectra of THz waveforms transmitted through metal pinholes, with diameters as labeled in the figure. These spectra are plotted on a log scale. Low frequencies are strongly attenuated as the aperture size decreases

As a result, these high-frequency components are more likely to transmit through a small aperture and reach the detector without substantial diffraction losses. These effects can be observed in transmission through simple apertures as well. Figure 12b shows the normalized spectra of THz pulses on a log scale, demonstrating the high-pass filtering of the radiation. Similar pulse reshaping effects have been reported with slit filters [44].

Near-field imaging techniques generally rely on the fact that the characteristic diffraction pattern of radiation transmitted through a small aperture develops only after a distance comparable to the wavelength of the radiation. In the THz range this implies that samples for near-field imaging must be thinner than a few hundred microns, and must be placed in close proximity to the near-field tip. Although these requirements are not as stringent as the analogous situation in optical near-field imaging, they are nonetheless important considerations which might preclude the use of near-field techniques in some applications.

Meanwhile two alternative approaches for THz near-field imaging have been explored, both based on the idea that the THz emission point is itself much smaller than the THz wavelength. One can take advantage of this fact by placing the sample close to the THz emitter, such that the radiation interacts with the sample before it has had time to diffract. Wynne and co-workers [45] have taken advantage of this to image a metallic test pattern deposited on an ZnTe crystal used for electro-optic THz generation, and Hunsche et al. [46] mapped out the extension of the near field of a photoconductive dipole antenna.

In this regard one should also mention the early work by Keilmann and co-workers who focused the radiation of a cw methanol laser into a similar near-field tip to spatially resolve the photoconductivity of a two-dimensional electron gas [47]. Yet, they did not take full images but determined the photoconductivity only at discrete spots on the sample. They also introduced tips of coaxial design which avoid the cutoff effect and allow for higher transmission. Furthermore Davidov et al. [48] used a specially designed resonant slit antenna for non-contact imaging with millimeter-waves. These antennas gave, however, a good resolution only in one dimension, making multiple scans along various direction and numerical data analysis inevitable.

5 Conclusions

We have described two important enhancements to the "T-ray" imaging system. The first, THz tomography, will be important in the eventual commercialization of the THz imaging technology, since the system will probably be configured for a reflection geometry. As the speed of waveform acquisition increases, it will become more challenging to rapidly analyze these data for image formation. The development of robust and reliable signal processing tools will be a necessary step in addressing this challenge. The results reported here demonstrate that it is possible to combine tomographic imaging with spectroscopic analysis. This possibility exploits the broadband nature of the radiation in two important ways: first, the short coherence length permits high-resolution tomography, and second, the spectroscopic information contained in the reflected pulses can be used for materials identification or characterization. The coherent nature of the THz radiation is also key, as it would not otherwise be possible to detect it with an unshielded room-temperature detector.

The application of optical near-field techniques to the THz imaging system is a nice example of the scale-invariance of Maxwell's equations. Aperture transmission and diffraction are phenomena which can be understood equally well, regardless of the wavelength of the radiation involved. As such, the results described here show improvements in spatial resolution which are consistent with those achieved with similar techniques in the visible region of the spectrum. Because of the high spatial coherence of the collimated THz beam, this system produces the best spatial resolution of any far-infrared imaging technique. This could be important in a number of areas, such as the application of T-ray imaging to the study of biological systems [49].

The work reported here represents only a small portion of the rapid progress that has occurred in this field during the last few years. This ultrafast pace holds great promise for both research and commercial applications.

Acknowledgements. We would like to acknowledge the contributions of Stefan Hunsche, Igal Brener and Martin C. Nuss of Bell Laboratories, Lucent Technologies. We also acknowledge the assistance of Fred Beisser of

Bell Laboratories in the fabrication of the near-field tip. Portions of this work were funded by the Air Force Research Laboratory (AFRL/PRKA), SBIR contract #F33615-98-C-2820, the National Science Foundation, grant #MIP-9457438, and by a joint grant from the Defense Advanced Research Projects Agency (DARPA) and the Air Force Office of Scientific Research (AFOSR), under grant #F49620-97-1-0513.

References

1. A. Nahata, D.H. Auston, T.F. Heinz: Appl. Phys. Lett. **68**, 150 (1996)
2. K. Kawase, M. Sato, T. Taniuchi, H. Ito: Appl. Phys. Lett. **68**, 2483 (1996)
3. S. Verghese, K.A. McIntosh, E.R. Brown: IEEE Trans. Microwave Th. Tech. **45**, 1301 (1997)
4. M.C. Nuss, P.C.M. Planken, I. Brener, H.G. Roskos, M.S.C. Luo, S.L. Chuang: Appl. Phys. B **58**, 249 (1994)
5. B.B. Hu, X.-C. Zhang, D.H. Auston: Phys. Rev. Lett. **67**, 2709 (1991)
6. L. Xu, X.-C. Zhang, D.H. Auston: Appl. Phys. Lett. **61**, 1784 (1992)
7. P.R. Smith, D.H. Auston, M.C. Nuss: IEEE J. Quantum Electron. **QE-24**, 255 (1988)
8. S.E. Ralph, S. Perkowitz, N. Katzenellenbogen, D. Grischkowsky: J. Opt. Soc. Am. B **11**, 2528 (1994)
9. Ch. Fattinger, D. Grischkowsky: Appl. Phys. Lett. **54**, 490 (1989)
10. Y. Cai, I. Brener, J. Lopata, J. Wynn, L. Pfeiffer, J. Federici: Appl. Phys. Lett. **71**, 2076 (1997)
11. M. van Exter, D. Grischkowsky: IEEE Trans. Microwave Th. Tech. **38**, 1684 (1990)
12. P. Uhd Jepsen, R.H. Jacobsen, S.R. Keiding: J. Opt. Soc. Am. B **13**, 2424 (1996)
13. R.A. Cheville, D. Grischkowsky: Opt. Lett. **20**, 1646 (1995)
14. B.I. Greene, P.N. Saeta, D.R. Dykaar, S. Schmitt-Rink, S.L. Chuang: IEEE J. Quantum Electron. **QE-28**, 2302 (1992)
15. G. Haran, W.-D. Sun, K. Wynne, R. Hochstrasser: Chem. Phys. Lett. **274**, 365 (1997)
16. B.B. Hu, M.C. Nuss: Opt. Lett. **20**, 1716 (1995)
17. D.M. Mittleman, R.H. Jacobsen, M.C. Nuss: IEEE J. Sel. Top. Quantum Electron. **2**, 679 (1996)
18. Q. Wu, F.G. Sun, P. Campbell, X.-C. Zhang: Appl. Phys. Lett. **68**, 3224 (1996)
19. T.S. Hartwick, D.T. Hodges, D.H. Barker, F.B. Foote: Appl. Opt. **15**, 1919 (1976)
20. A.J. Cantor, P.K. Cheo, M.C. Foster, L.A. Newman: IEEE J. Quantum Electron. **QE-17**, 477 (1981)
21. N. Gopalsami, S. Bakhtiari, S.L. Dieckman, A.C. Raptis, M.J. Lepper: Mater. Eval. **52**, 412 (1994)
22. N.C. Currie, F.J. Demma, D.D. Ferris Jr., R.W. McMillan, V.C. Vannicola, M.C. Wicks: Proc. SPIE **2567**, 124 (1995)
23. G. Rehm, U. Guckenberger, K. Huber, H. Brand: In Proceedings of the 5th International Workshop on Terahertz Electronics (Grenoble, France, Sept. 1997)
24. D. Grischkowsky, S. Keiding, M. van Exter, Ch. Fattinger: J. Opt. Soc. Am. B **7**, 2006 (1990)
25. J.R. Birch: Infr. Phys. **30**, 195 (1990)
26. D.M. Mittleman, J. Cunningham, M.C. Nuss, M. Geva: Appl. Phys. Lett. **71**, 16 (1997)
27. D.M. Mittleman, S. Hunsche, L. Boivin, M.C. Nuss: Opt. Lett. **22**, 904 (1997)
28. R.A. Cheville, D. Grischkowsky: Appl. Phys. Lett. **67**, 1960 (1995)
29. M. van Exter, Ch. Fattinger, D. Grischkowsky: Opt. Lett. **14**, 1128 (1989)
30. A.E. Siegman: *Lasers*, Chapt. 17 (University Science Books, Mill Valley, CA 1986)
31. J.R. Birch: Infr. Phys. **33**, 33 (1992)
32. A.B. Ruffin, J.F. Whitaker, S. Feng, H.G. Winful, J.V. Rudd: Direct observation of the Gouy phase shift with single-cycle terahertz pulses, Conference on Lasers and Electro-Optics, invited presentation (1999)
33. R.A. Cheville, R.W. McGowan, D. Grischkowsky: Phys. Rev. Lett. **80**, 269 (1998)
34. D.M. Mittleman, R.H. Jacobsen, R. Neelamani, R.G. Baraniuk, M.C. Nuss: Appl. Phys. B **67**, 379 (1998)
35. A. Oppenheim, R. Schafer: *Discrete-Time Signal Processing* (Prentice-Hall, New York 1989)
36. D. Donoho: Appl. Comp. Harm. Anal. **2**, 101 (1995)
37. L. Duvillaret, F. Garet, J.-L. Coutaz: IEEE J. Sel. Topics Quantum Electron. **2**, 739 (1996)
38. Z.B. Niazi, T.J. Essex, R. Papini, D. Scott, N.R. McLean, M.J. Black: Burns **19**, 485 (1993)
39. L. Thrane, R.H. Jacobsen, P. Uhd Jepsen, S.R. Keiding: Chem. Phys. Lett. **240**, 330 (1995)
40. S. Hunsche, M. Koch, I. Brener, M.C. Nuss: Opt. Commun. **150**, 22 (1998)
41. D.W. Pohl: In *Advances in Optical and Electron Microscopy* (Academic Press, New York 1991)
42. E. Betzig, J.K. Trautmann: Science **257**, 189 (1992), and references therein
43. S. Hunsche, M. Koch, I. Brener, M.C. Nuss: In Conference on Lasers and Electro-Optics, **11**, 1997 OSA Technical Digest Series (Optical Society of America, Washington DC 1997) p. 64
44. J. Bromage, S. Radic, G.P. Agrawal, C.R. Stroud Jr., P.M. Fauchet, R. Sobolewski: Opt. Lett. **22**, 627 (1997)
45. K. Wynne, D.A. Jaroszynski: Opt. Lett. **24**, 25 (1999)
46. S. Hunsche, Y. Cai, I. Brener, M.C. Nuss, J. Wynn, J. Lopata, L. Pfeiffer: In Conference on Lasers and Electro-Optics, **6**, 1998 OSA Technical Digest Series (Optical Society of America, Washington DC 1998) p. 64
47. R. Merz, F. Keilmann, R.J. Haug, K. Ploog: Phys. Rev. Lett. **70**, 651 (1993)
48. M. Golosovsky, D. Davidov: Appl. Phys. Lett. **68**, 1579 (1996)
49. M. Koch, S. Hunsche, P. Schumacher, M.C. Nuss, J. Feldmann, J. Fromm: J. Wood Sci. Tech. **32**, 421 (1998)